

Impact of embedded ^{163}Ho on the performance of the transition-edge sensor microcalorimeters of the HOLMES experiment

Douglas Bennett¹, Matteo Borghesi^{5,6}, Pietro Campana^{5,6}, Rodolfo Carobene^{5,6}, Giancarlo Ceruti⁶, Matteo De Gerone³, Marco Faverezani^{5,6}, Lorenzo Ferrari Barusso^{3,4}, Elena Ferri⁶, Joseph Fowler¹, Sara Gamba^{5,6}, Flavio Gatti^{3,4}, Andrea Giachero^{5,6}, Marco Gobbo^{5,6}, Danilo Labranca^{5,6}, Roberto Moretti^{5,6}, Angelo Nucciotti^{a,5,6}, Luca Origo⁶, Stefano Ragazzi^{5,6}, Dan Schmidt^{b,1}, Daniel Swetz¹, Joel Ullom^{1,2}

¹ National Institute of Standards and Technology (NIST), Boulder, Colorado, USA

² University of Colorado, Boulder, Colorado, USA

³ Istituto Nazionale di Fisica Nucleare (INFN), Sezione di Genova, Genova, Italy

⁴ Dipartimento di Fisica, Università di Genova, Genova, Italy

⁵ Dipartimento di Fisica, Università di Milano-Bicocca, Milano, Italy

⁶ Istituto Nazionale di Fisica Nucleare (INFN), Sezione di Milano Bicocca, Milano, Italy

Received: date / Accepted: date

Abstract We present a detailed investigation of the performance of transition-edge sensor (TES) microcalorimeters with ^{163}Ho atoms embedded by ion implantation, as part of the HOLMES experiment aimed at neutrino mass determination. The inclusion of ^{163}Ho atoms introduces an excess heat capacity due to a pronounced Schottky anomaly, which can affect the detector's energy resolution, signal height, and response time. We fabricated TES arrays with varying levels of ^{163}Ho activity and characterized their performance in terms of energy resolution, decay time constants, and heat capacity. The intrinsic energy resolution was found to degrade with increasing ^{163}Ho activity, consistent with the expected scaling of heat capacity. From the analysis, we determined the specific heat capacity of ^{163}Ho to be $(2.9 \pm 0.4(\text{stat}) \pm 0.7(\text{sys}))$ J/K/mol at (94 ± 1) mK, close to the literature values for metallic holmium. No additional long decay time constants correlated with ^{163}Ho activity were observed, indicating that the excess heat capacity does not introduce weakly coupled thermodynamic systems. These results suggest that our present TES microcalorimeters can tolerate ^{163}Ho activities up to approximately 5 Bq without significant performance degradation. For higher activities, reducing the TES transition temperature is necessary to maintain energy resolution. These findings provide critical insights for optimizing TES microcalorimeters for future neutrino mass experiments and other applications requiring embedded radioactive sources. The study also highlights the robustness of TES technology in handling implanted radionuclides while maintaining high-resolution performance.

1 Introduction

Calorimetric measurement of the fraction of energy released in nuclear beta decays that is not carried away by neutrinos was originally proposed to overcome the limitations of external-source spectrometric neutrino mass experiments with tritium [1] and ^{163}Ho [2]. Pioneering neutrino mass calorimetric experiments have been performed with tritium ions implanted in Si(Li) [1] and HPGe [3] detectors, with ^{163}Ho ions implanted in HPGe [4] detectors, and with a high-temperature gas proportional detector containing a gaseous organometallic holmium compound [5]. In those early experiments based on standard detector technologies, sensitivity was limited by the energy resolution and possibly by solid-state effects [6]. The advent of sensitive low-temperature detectors (LTDs) has provided new opportunities to improve calorimetric experiments [7] and has expanded the choice of source isotopes. Besides some attempts to use ion-implanted tritium [8, 9], early neutrino mass experiments with LTDs focused on the low Q beta decay of ^{187}Re in both metallic rhenium [10] and dielectric AgReO_4 [11] energy absorbers. However, the very low specific activity of rhenium (^{187}Re , half-life $\sim 4 \times 10^{10}$ years) made scaling up these experiments impractical [7]. In contrast, the much shorter half-life of electron-capture ^{163}Ho (about 4750 years) makes it preferable for LTD-based calorimetric experiments, requiring only 10^{11} nuclei per 1 decay/sec. Several approaches have been explored for the inclusion of the ^{163}Ho source in the absorbers, including the encapsulation by epoxy drops contained in folded tin foils [12], the inclusion of holmium in superconducting yttrium compounds [13], or the drying of a holmium-containing solution dripped onto nanoporous

^ae-mail: angelo.nucciotti@mib.infn.it

^be-mail: dan.schmidt@nist.gov

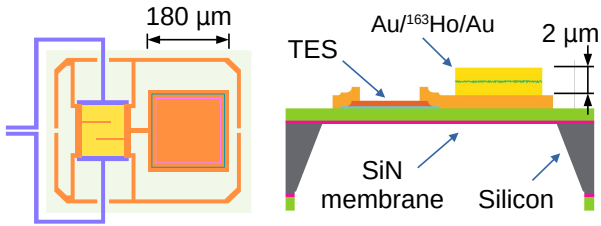


Fig. 1 Left: Layout of the TES microcalorimeter, showing the side-by-side Mo/Cu bilayer sensor and gold absorber, with a copper perimeter for enhanced thermal conduction [24]. Right: Schematic (not to scale) of the micromachined TES microcalorimeter with embedded ^{163}Ho as used in this work.

gold [14]. However, the most promising technique to date remains ion implantation of ^{163}Ho , adopted by the ECHO [15] and HOLMES [16] neutrino mass experiments. Radioactive sources have been embedded in LTD absorbers—mainly via ion implantation—for applications such as ^7Be electron-capture studies for sterile neutrino searches [17], astrophysical process investigations [18], and total decay energy spectroscopy for metrology, safeguards, and other purposes [19]. Recently, tritium generated in LiF LTDs by neutron capture has also been used for sterile neutrino searches [20].

2 Transition-edge Sensor Microcalorimeters for HOLMES

The HOLMES experiment uses transition-edge sensor (TES) microcalorimeters [21] whose design and fabrication details are described here and in Appendix B. In this paper we also investigate how the inclusion of ^{163}Ho atoms affects the detector response.

The TES [21] microcalorimeters used for this work are specifically designed [22] to meet the experimental requirements of HOLMES. Mo/Cu bilayer TESs are tuned to have critical temperatures around 95 mK and are thermally coupled via a thin-film copper link to a $180 \times 180 \times 2 \mu\text{m}^3$ gold absorber, in which the ^{163}Ho is embedded by ion implantation (Fig. 1). HOLMES microcalorimeters are designed with the absorber positioned beside the sensor to prevent proximity [23]. Detectors are suspended on a SiN_x membrane to provide a finite thermal link G to the thermal bath, which is kept at a constant temperature of 40 mK. Additional copper banks are inserted to increase G and to control the TES resistance and excess noise [22, 24, 25].

The detectors operate as thermal equilibrium calorimeters [26], where all energy deposited in the absorber is converted into a thermal signal. In the simplest model, the system is treated as a single heat capacity – the sum of absorber and TES electron contributions – characterized by the TES electron temperature. Both signal amplitude and decay time constant depend on this total heat capacity. For accurate performance predictions, electrothermal feedback from

constant-voltage TES biasing must be included, as described by the full electrothermal model [21]. Here, we use its small-signal approximation.

For a holmium-based neutrino mass experiment with approximately 1000 detectors to accumulate sufficient statistics to reach neutrino mass sensitivities below $1 \text{ eV}/c^2$, it is desirable to have per detector activities of several hundred decays per second [27]. Therefore, it is critical to assess the impact of doping on detector performance. In fact, sensitivity would be adversely affected by excessive deterioration of energy resolution or increase in dead time [27, 28]. The experiment’s dead time is determined by the signal fall time, as any new event occurring during the decay of a previous pulse results in both events being discarded from analysis. Since the fall time is proportional to the heat capacity (C), an increased heat capacity leads to longer dead times. Furthermore, the heat capacity directly impacts the achievable energy resolution: for negligible readout noise and in the regime of strong electrothermal feedback, the energy resolution scales as \sqrt{C} , so a larger heat capacity results in poorer energy resolution [21]. In contrast, the rise time of the signals is primarily determined by the electrical cutoff set by $L/R_0 \approx 20 \mu\text{s}$, where R_0 is the sensor resistance at its operating point and L is the inductance of the bias circuit. The rise time is related to the detector resolving time and therefore determines the level of background at the end-point caused by ^{163}Ho decays occurring too close in time to be resolved [27].

Holmium it is known to exhibit an excess heat capacity due to a pronounced Schottky anomaly [29]. Hyperfine [29] and crystalline field [30] splittings are caused by $4f$ atomic electrons interacting with ^{163}Ho nuclear spins ($I = 7/2$) and with electric field gradients in the fcc lattice of the gold host, respectively. These splittings induce Schottky anomalies in the heat capacity of the ^{163}Ho nuclei which are expected to peak between 0.1 K and 1 K, i.e., near the operating temperature of HOLMES detectors. As a result, microcalorimeters loaded with large amounts of ^{163}Ho are expected to show degraded performance. By studying detector parameters such as the energy resolution and the decay time at varying ^{163}Ho activities, it becomes possible to estimate the specific heat capacity contributed by the presence of holmium.

Depending on the strength of the coupling between the detector electronic system and the ^{163}Ho nuclei ensemble, this excess heat capacity can cause either an increase of the total detector heat capacity or the appearance of an additional weakly coupled thermodynamic system. Therefore, depending on the ^{163}Ho concentration and on the detector operating temperature, the ^{163}Ho doping can manifest as a reduction in signal height, a worsening of detector resolution, a slowing of detector response or a complex signal shape with additional long decay times.

The heat capacity of metallic holmium has been measured to be 3.8 J/K/mol [29] at 95 mK and the amount of ^{163}Ho to be added in the detectors for a unit activity is 1.1×10^{11} nuclei, or 3.6×10^{-13} moles. For comparison, the total heat capacity of HOLMES microcalorimeters at the same temperature is estimated to be about $8 \times 10^{-13} \text{ J/K}$ [22]. A first investigation of the impact of ^{163}Ho doping in magnetic metallic microcalorimeters was reported by the ECHO collaboration [31, 32].

The HOLMES detectors are manufactured using a combination of thin-film fabrication techniques and silicon micromachining. The ^{163}Ho atoms are embedded in the detectors during fabrication using ion implantation and then encapsulated with a final layer of Au. Detectors are grouped in 64 pixel arrays contained on individual silicon die (Fig. 2). Details of the fabrication and implantation are given in Appendix A and Appendix B.

3 Experimental Methods and Detector Characterization

The data presented in this work are taken with microcalorimeters belonging to three arrays. The first array (Array 0) was fabricated without ion implantation to verify that the fabrication process developed for encapsulation yields devices with performance matching those in [22], which were produced in a single step using DRIE micromachining at NIST. The other two arrays – Arrays 1 and 2 – differ in their ion implantation protocols (see Appendix A), with detector activities ranging from 0 up to about 1 Bq and 0.6 Bq, respectively.

All measurements were conducted in a dilution refrigerator, where the copper boxes hosting the arrays (see Fig. 2) were maintained at a stable temperature of 40 mK. For detector calibration, a fluorescence source was used, consisting of a primary ^{55}Fe source that irradiated a target composed of sodium chloride, calcium carbonate, and aluminum. The resulting $K\alpha$ X-rays from aluminum (1486 eV), chlorine (2622 eV), calcium (3690 eV), and manganese (5900 eV) were used as calibration points. For Arrays 1 and 2 containing ^{163}Ho , the spectra also exhibit prominent peaks corresponding to the calorimetric detection of atomic de-excitation energy from dysprosium atoms left with core holes following electron capture [33]. The most intense are the N1 and M1 capture peaks, at approximately 412 eV and 2041 eV, respectively. Each detector is characterized by acquiring IV curves at various heat bath temperatures T_b , measured using a calibrated RuO_x thermometer. From these measurements, the thermal conductance $G(T)$ is extracted and parametrized as $G(T) = ngT^{n-1}$, where n and g are obtained from a fit to the data. The optimal operating point parameters, specifically the TES current I_0 at a resistance R_0 set to approximately 30% of the normal-state value, are

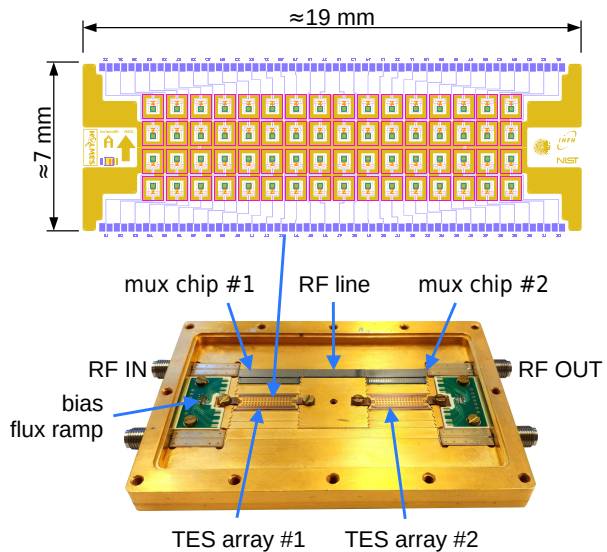


Fig. 2 Top: Layout of one of the two 16×4 pixel arrays fabricated on $14 \times 19 \text{ mm}^2$ chips. Each cell reproduces the layout shown in Fig. 1 (Left). Bottom: Copper box used for characterizing Arrays 0 and 1. The TES arrays are mounted at the center. Only the upper half of the arrays (32 microcalorimeters) is instrumented with the bias network and microwave multiplexer chips. The multiplexers have their feedlines aligned with the SMA connectors and the central interconnecting feedline. The box is closed with a light-tight cover featuring two openings above the array, each shielded by a $6 \mu\text{m}$ aluminum foil, to allow irradiation with an external X-ray source. For Array 2, a new box accommodating a single array was used (see figure in [33]).

also determined. For each detector, the operating temperature T_0 is then obtained from $P_{J0} = I_0^2 R_0$ using the relation $P_{J0} = g(T^n - T_b^n)$ and $T_0 \approx 95 \text{ mK}$.

Pulses acquired at the optimal working point are triggered offline and then processed to reject spurious pulses, to correct for gain drifts, and to estimate the amplitude by optimal filtering [34] and other parameters, such as pulse time constants [35]. Pulse amplitude spectra are energy calibrated by interpolating the X-ray peaks with a quadratic model forced through the origin. The detector activity is estimated from the integral of the M1 peak¹.

Tab. 1 summarizes the properties and performance of the TES microcalorimeters in the three arrays discussed here and compares them with previously reported results [22].

4 Results

Pulses recorded at the N1 peaks (Fig. 3) in the two implanted arrays are well described by a double exponential model with a rise and fall time. However, a slight deviation from the simple exponential behavior is observed at the start of the decay, likely due to the breakdown of the small signal

¹The M1 branching ratio is determined from a high-statistics measurement of the full spectrum. Detailed results on the full EC spectral shape will be discussed in a forthcoming publication.

Table 1 Summary of array parameters and performance. Time constants τ_{rise} and τ_{dec} refer to low-energy signals (e.g., Al X-rays or N1 ^{163}Ho capture). Except for G , all values are for TESs with minimal or no implanted activity. Intrinsic detector resolutions ΔE_0 are calculated from Eq. (4), while ΔE_{FWHM} are the FWHMs obtained by fitting the Mn $K\alpha$ peaks. Note that performance comparisons should account for differences in bath and operating temperatures.

Array	ΔE_0 [eV]	ΔE_{FWHM} [eV]	τ_{rise} [μs]	τ_{dec} [μs]	G [pW/K] ^a
TESs in [22]	3.3	4.5 ± 0.1	13	54(220) ^b	600
0 ^c	3.7	4.2 ± 0.1	15	300	387 ± 57
1 ^d	4.8	5.8 ± 0.1	9	360	---
2 ^e	5.0	6.5 ± 0.1	8	600	171 ± 26

^a See also comments in Appendix B

^b Fast pulses in [22] are modeled with two exponential decays. The first value represents the main decay time constant, while the second (in parentheses) corresponds to the long decay component. Bath and detector working temperatures were 60 mK and 100 mK, respectively.

^c Values reported are for the pixel with the best energy resolution. Bath and detector working temperatures were 60 mK and 100 mK, respectively.

^d G was not measured for this array. Energy resolutions and time constants are for the best-performing pixel with minimal activity (about 0.04 Bq). Bath and detector working temperatures were 40 mK and 95 mK, respectively.

^e G was measured only for pixels in one half of the array. Energy resolutions and time constants are for the best-performing pixel with minimal activity (around 0.1 Bq). Bath and detector working temperatures were 40 mK and 95 mK, respectively.

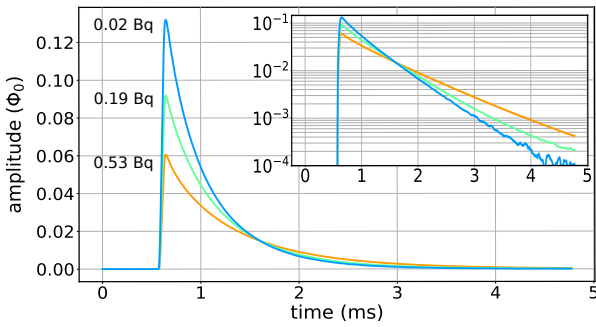


Fig. 3 Averaged pulses from N1 capture events in pixels with about 0.02 Bq, 0.2 Bq, and 0.5 Bq of ^{163}Ho activity from Array 2. The logarithmic scale in the inset highlights the absence of additional long decay time constants.

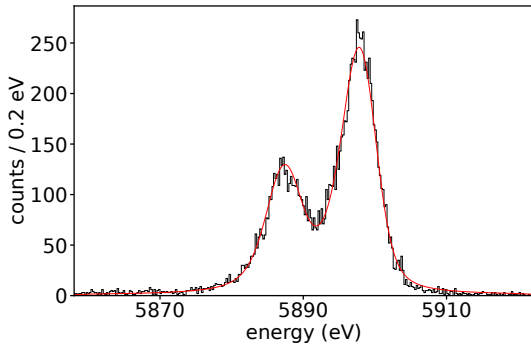


Fig. 4 Mn $K\alpha$ X-ray peak measured with the best pixel in Array 0. The FWHM energy resolution is (4.2 ± 0.1) eV, while the intrinsic resolution, calculated from Eq. (4), is about 3.7 eV.

approximation. Furthermore, aside from the primary exponential decay time constants, which range between approximately 600 μs and 900 μs , no additional long time constants correlated with the implanted activities are observed in the pulses.

The energy resolution is evaluated using the Mn $K\alpha$ peak, leveraging its high-statistics data across all three arrays. For improved precision, the local energy scale is calibrated using the Mn $K\alpha_1$ and $K\alpha_2$ peaks [36]. Fig. 4 shows the Mn $K\alpha$ peak resolution for the best pixel in Array 0. Mn $K\alpha$ peak spectra from detectors with comparable activity and energy resolution were summed to improve statistics. The resulting spectra were then fitted using the method described in [37] to investigate the presence of peak tails potentially associated with holmium implantation. Refer to Fig. 5 for details on the spectra. The red curves represent the fitted model, including Gaussian peaks for all seven Mn $K\alpha$ components [36], while the blue curves show the flat background model, which correlates with the Mn $K\alpha$ peak intensity but not with the implanted activity. This background, caused by X-rays interacting outside the absorber, appears only on the low-energy side of the peaks and has a level of approximately $A_{tail}(K\alpha) \times 0.006$ counts/eV, where $A_{tail}(K\alpha)$ is the total peak amplitude. The green curves show the sum of all Gaussian components. Including an exponential tail component as in [37], with a scale parameter λ_{tail} ranging from 0.1 eV to 100 eV⁻¹, does not improve the fit. The tail amplitude is always negligible, at most 0.1% of the total Gaussian amplitude, and shows no correlation with the implanted activity.

All TESs are found to be well in the extreme electro-thermal feedback (ETF) regime as

$$\mathcal{L}_1 = \frac{I_0^2 R_0 \alpha_I}{GT_0} \gg 1 \quad (1)$$

where α_I , the TES's logarithmic constant current temperature sensitivity, is not directly assessed for the TESs under test, but it is expected to be about 100 with a 30% 1σ uncertainty.

The decay time constant is found fitting pulses from the N1 peak of the ^{163}Ho spectrum to remain in the small sig-

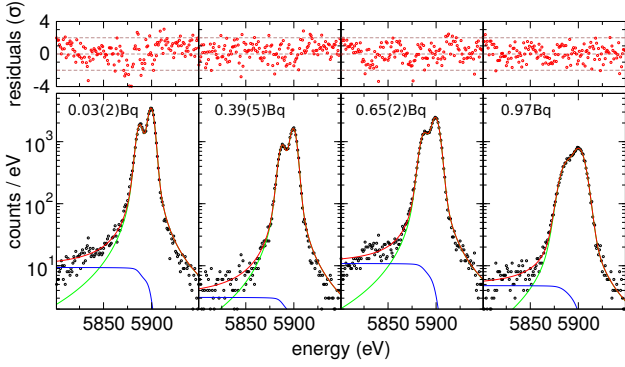


Fig. 5 The four panels from left to right show the Mn $K\alpha$ peaks obtained summing spectra from a few pixels with increasing activity. The FWHM energy resolutions obtained fitting the Mn $K\alpha$ peaks from left to right are 6.5 ± 0.1 , 6.9 ± 0.1 , 8.5 ± 0.1 and 13.1 ± 0.1 eV. Red curves show the fitted model with Gaussian peaks for all seven Mn $K\alpha$ components [36]; blue curves show the flat background; green curves represent the sum of all Gaussians.

nal limit. Considering also that the detectors are in the low inductance limit, the decay time constant is expected [21] to be

$$\tau_{dec} = \frac{C}{G} \frac{1 + \beta_I + R_L/R_0}{1 + \beta_I + R_L/R_0 + (1 - R_L/R_0)\mathcal{L}_I} = \eta \frac{C}{G} \quad (2)$$

where R_L and β_I are the reference (or load) resistor and the TES's logarithmic current sensitivity at constant current. Also β_I is only known from the characterization of similar devices to be around 2 with a 50% 1σ uncertainty.

In the strong ETF regime and with negligible amplifier noise, the detector intrinsic FWHM energy resolution is expected [21] to be

$$\Delta E_0 = 2\sqrt{2\ln 2} \sqrt{4k_B T_b^2 \frac{C}{\alpha_I} \sqrt{n/2}} \quad (3)$$

The intrinsic energy resolution for each pixel is calculated by integrating the power spectral density of the noise, $S_{pow}(f)$ [21]:

$$\Delta E_0 = 2\sqrt{2\ln 2} \sqrt{\int_0^\infty \frac{4}{S_{pow}(f)} df}. \quad (4)$$

Here, $S_{pow}(f)$ is obtained by averaging the Fourier transform of noise waveforms and using the detector's current-to-power responsivity, derived from the average pulse shape and amplitude for known small energies (small signal limit). In both eq. (2) and eq. (3), C is the total heat capacity of the detector at the working temperature T_0 . To interpret the data we assume that

$$C(A_{Ho}) = C_{TES} + C_{Ho} = C_{TES} + n_{Ho} c_{Ho} = C_{TES} + \frac{A_{Ho}}{\lambda N_A} c_{Ho} \quad (5)$$

where C_{TES} is the combined heat capacity of the TES sensor and the absorber – estimated to be approximately 0.8×10^{-12} J/K at around 90 mK and refined to (1.0 ± 0.3) pJ/K based on Array 0 data using eq. (2) – and n_{Ho} , c_{Ho} , A_{Ho} , and

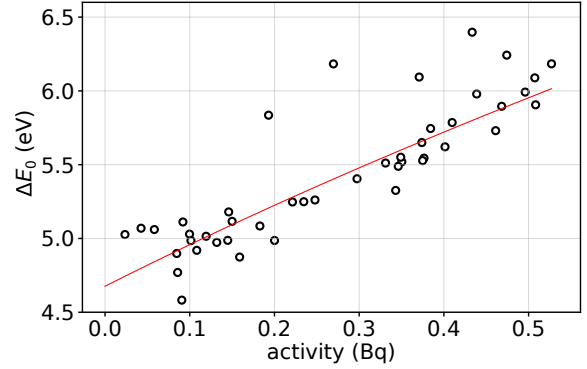


Fig. 6 Plot of ΔE_0 versus A_{Ho} for Array 2. Intrinsic resolutions are derived using Eq. (4) as described in the text. Pixel activities are calculated from the M1 peak integral, using its branching ratio from the full ^{163}Ho spectrum analysis, to be detailed in an upcoming publication. The solid line represents the robust fit to the data.

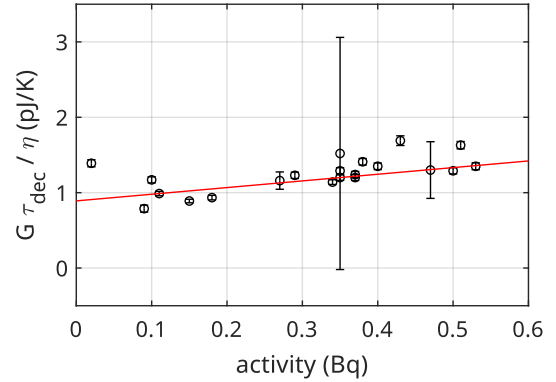


Fig. 7 Plot of $\tau_{dec}G/\eta$ versus A_{Ho} for one half of the pixels in Array 2. Error bars reflect the propagated uncertainties of all parameters in eq. (2). The solid line shows the result of a robust linear fit to the data.

λ represent the number of moles, the specific heat capacity in J/K/mol, the implanted activity in the detector in Bq, and the decay constant of ^{163}Ho ($4.6 \times 10^{-12} s^{-1}$), respectively.

Considering $C(A_{Ho})$ as given by Eq. 5, we extracted c_{Ho} by fitting ΔE_0 from Eq. (4) as a function of A_{Ho} in Fig. 6, using the model $y(A) = a\sqrt{C_{TES}} + bA_{Ho}$ (from Eq. 3), where $a \propto \sqrt{T_b^2 \sqrt{n}/\alpha_I}$ and $b = c_{Ho}/(\lambda N_A)$ are free parameters. The solid line in Fig. 6 shows the result of a robust fit, yielding $c_{Ho} = \lambda N_A b = (2.9 \pm 0.4(\text{stat}) \pm 0.7(\text{sys}))$ J/K/mol at (94 ± 1) mK. This value is slightly lower than, but consistent with, the literature value for the heat capacity of metallic holmium (3.8 J/K/mol [29]). The statistical uncertainty reflects pixel-to-pixel variations in the parameters of eq. (3), while the systematic uncertainty is dominated by the uncertainty in C_{TES} , estimated to range between 0.6 pJ/K and 1.0 pJ/K.

For the derivation of c_{Ho} from exponential decay time constant of N1 pulses, we plot $\tau_{dec}G/\eta$ versus the pixel activity A_{Ho} as in Fig. 7. Here the error bars are obtained

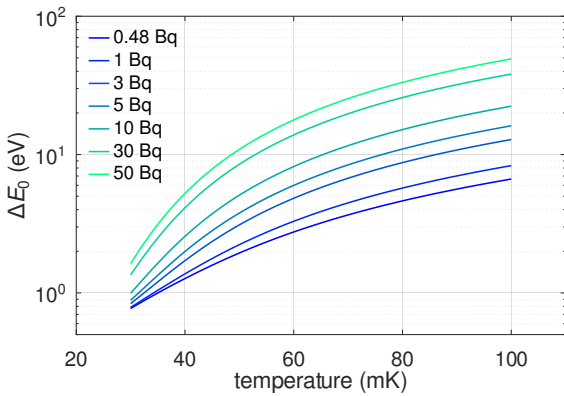


Fig. 8 Projected intrinsic energy resolution ΔE_0 as a function of TES operating temperature for different ^{163}Ho activities. Curves are normalized to 6 eV FWHM at 0.5 Bq and 90 mK (average activity and energy resolution of Array 2 [33]). Calculations assume C_{TES} scales with T , c_{Ho} from [29], and that detector design can be optimized to maintain G and α_I at suitable values for each temperature. In particular, α_I is assumed to remain at least 100 and the decay time constant is kept on the order of 100 μs .

propagating the errors on all parameters appearing in eq. (2) and are dominated by the uncertainty on α_I . A robust linear interpolation gives $C_{\text{TES}} = (0.89 \pm 0.08)$ pJ/K and $c_{\text{Ho}} = (4.7 \pm 1.3)$ J/K/mol.

5 Discussion

The values obtained for c_{Ho} are consistent with each other and align with those reported by ECHO [32] and for metallic holmium [29]. Given its reduced sensitivity to α_I and β_I , we consider the result derived from ΔE_0 to be the most robust. Notably, the significance of our findings arises from the distinct physical mechanisms governing signal formation in TES detectors compared to previous studies [32].

Array 2 has been used for taking high statistics data with the aim of performing an analysis of the ^{163}Ho decay end point to derive a limit on the neutrino mass [33]. Improving the neutrino mass sensitivity requires measurements of even more decays through a combination of more detectors and higher per pixel ^{163}Ho activity, without significantly degrading energy resolution. Monte Carlo simulations [27] indicate that the impact on neutrino mass sensitivity remains negligible as long as the energy resolution is better than 10 eV.

The extrapolation of the fit in Fig. 6 suggests that the energy resolution will not be significantly affected by the ^{163}Ho activity, as long as the activity is kept below about 5 Bq per detector. A further increase of the activity requires a reduction of the TES operating temperature. Fig. 8 illustrates the expected scaling of the intrinsic energy resolution ΔE_0 on TES operating temperature and implanted ^{163}Ho activity, based on the assumptions detailed in the caption. It is

apparent that to operate detectors with about 50 Bq without performance degradation, the operating temperature must be reduced to about 40 mK.

6 Conclusions

In summary, this work demonstrates that embedding ^{163}Ho in the absorber of TES microcalorimeters at activities up to approximately 1 Bq results solely in an increased heat capacity, with no evidence of non-Gaussian response or additional thermally decoupled systems. Despite the relatively low ^{163}Ho concentration in the gold absorber, the measured specific heat capacity is consistent with values reported for metallic holmium. Extrapolation of our results indicates that, to achieve detector activities as high as 50 Bq without significant degradation in performance, the microcalorimeters must be redesigned to operate at temperatures as low as 40 mK.

Acknowledgements This work and the HOLMES experiment have been supported by Istituto Nazionale di Fisica Nucleare (INFN) and by European Research Council under the European Union’s Seventh Framework Programme (FP7/2007–2013)/ERC Grant Agreement no. 340321.

Declarations

Conflict of interest The authors have no competing interests to declare that are relevant to the content of this article.

Availability of data and materials Data available from the corresponding authors upon reasonable request.

Authors’ contributions

Conceptualization: Matteo Borghesi, Matteo De Gerone, Marco Faverezani, Elena Ferri, Flavio Gatti, Andrea Giachero, Lorenzo Ferrari Barusso, Angelo Nucciotti, Luca Origo, Dan Schmidt, Joel Ullom, Sara Gamba; Investigation: Matteo Borghesi, Marco Faverezani, Elena Ferri, Sara Gamba, Luca Origo; Formal Analysis: Matteo Borghesi, Elena Ferri, Luca Origo, Angelo Nucciotti; Software: Matteo Borghesi, Pietro Campana, Rodolfo Carobene, Joseph Fowler, Sara Gamba, Andrea Giachero, Roberto Moretti, Luca Origo; Data Curation: Matteo Borghesi, Marco Faverezani, Elena Ferri; Visualization: Marco Gobbo, Danilo Labranca, Luca Origo; Resources: Douglas Bennett, Giancarlo Ceruti, Matteo De Gerone, Lorenzo Ferrari Barusso, Dan Schmidt; Supervision: Flavio Gatti, Stefano Ragazzi, Daniel Swetz, Joel Ullom, Angelo Nucciotti; Funding Acquisition: Matteo De Gerone, Marco Faverezani, Flavio Gatti, Stefano Ragazzi, Joel Ullom; Project Administration: Angelo Nucciotti; Writing-Original Draft Preparation:

Marco Faverzani, Elena Ferri, Andrea Giachero, Angelo Nucciotti; Writing-Review & Editing: Douglas Bennett, Matteo Borghesi, Pietro Campana, Rodolfo Carobene, Matteo De Gerone, Joseph Fowler, Sara Gamba, Marco Gobbo, Danilo Labranca, Roberto Moretti, Angelo Nucciotti, Dan Schmidt, Daniel Swetz, Joel Ullom;

Appendix A: ^{163}Ho isotope embedding

The ^{163}Ho nuclei for the HOLMES experiments are produced by irradiating ^{162}Er enriched Er_2O_3 samples in a flux of thermal neutrons [38]. The irradiated samples are then chemically purified by ion exchange chromatography to separate other chemical species produced by nuclear reactions in the reactor [38]. The final samples still contain traces of ^{165}Ho (≈ 2 $^{163}/^{165}\text{Ho}$ at. ratio) and ^{166m}Ho ($\approx 2 \times 10^3$ $^{163}/^{166m}\text{Ho}$ at. ratio) which must be removed to prevent extra contributions to the detector heat capacity and, in the case of the beta decaying ^{166m}Ho , to limit background counts interfering with the neutrino mass measurement. The ^{163}Ho nuclei are introduced in HOLMES microcalorimeters by ion implantation [39]. A holmium ion current is produced by a hot-running cold plasma sputter ion source. Ions are accelerated to 30 keV and the 163 mass component of the beam is selected by a solenoid magnet and an adjustable slit at the beam waist. When it reaches the detector array, the beam has an approximately 2D gaussian cross-section with a FWHM of about 4 mm. The deflected 165 and 166 mass ions are separated from the 163 mass one by about 7 and 11 σ s, respectively, and are almost completely masked by the slit. Based on SRIM² simulations of the implantation profile, we estimate an approximate holmium concentration of $x_{\text{Ho}} \approx 0.15\%$ for a ^{163}Ho activity of 1 Bq.

Arrays 1 and 2 (see Section 3) differ in their ion implantation protocols. Array 1 was ion-implanted with a single central shot, targeting a nominal peak activity of approximately 4 Bq. Array 2 received four implantation shots, designed to achieve a more uniform activity distribution with a nominal maximum of about 2 Bq. Due to the unavoidable sputtering effect of the ion beam, SRIM simulations indicate that the actual detector activity should saturate at around 2 Bq. However, for reasons not yet fully understood, the highest measured activity was approximately 1 Bq. Each beam shot was performed with ^{163}Ho ion currents of approximately 10 nA for several thousand seconds.

Appendix B: Microcalorimeter array fabrication

HOLMES microcalorimeters are arranged in 64 pixel arrays fabricated at different institutions of the HOLMES collab-

oration [35]. NIST carries out the fabrication without performing the silicon micromachining to release the SiN membranes with the detectors on top. At this stage, only the bottom gold layer of the absorber, 1 μm thick, is deposited. The wafer is then cut into $14 \times 19 \text{ mm}^2$ chips containing two arrays each. To allow further processing the chips have masks on both sides. On the detector side, a photoresist lift-off mask is left to complete the detector absorbers. On the back of the chip a SiN mask is patterned to allow anisotropic silicon etching to release the membranes. Subsequent fabrication steps are performed at the INFN laboratories of the Universities of Genova and Milano-Bicocca. After ion implanting the ^{163}Ho in the bottom gold layer with a depth profile extending about 10 nm, the top gold layer – 1 μm thick – is deposited in an ion beam assisted sputtering system. The use of four symmetric ion beams and gold targets gives a uniform – 4% spread on a $10 \times 10 \text{ mm}^2$ sample – gold deposition on the array surfaces at a rate of more than 100 nm/h. After the second Au layer is completed and the ^{163}Ho is completely encapsulated, the chip is dipped in an acetone bath at 50 $^\circ\text{C}$ for 2 hours to perform the lift-off process. Finally, the chip is mounted in a EPDM o-ring sealed POM holder with only the back exposed and it is dipped in a KOH bath at 80 $^\circ\text{C}$ for about 5 hours, until the SiN membranes are completely released by the anisotropic etching. As shown in Table 1, and corroborated by the decay time constants, all three arrays exhibit a G smaller than expected based on the data reported in [22], with significant variation across the arrays. This discrepancy is likely attributable to the KOH processing used for these devices, as opposed to the DRIE process employed in [22]. While the exact mechanism remains unclear, the variation appears to stem from bubble formation and trapping during the silicon etching in the KOH soaking process.

Appendix C: Array readout

These arrays were mounted in gold-plated copper boxes (see Fig. 2), which also house the circuitry for biasing the detectors, along with the multiplexing chips for signal readout. The electrical connections between the multiplexing chips are established using superconducting aluminum bonding wires, each with a diameter of 25 μm . To ensure proper thermal contact between the sub-array and the copper holder, ~ 20 gold bonding wires, each 50 μm in diameter, were also employed.

The signals from the voltage-biased TES arrays are frequency-multiplexed in the 4–8 GHz band using flux ramp-linearized rfSQUIDS [40]. Each multiplexing chip handles 32 detector channels, distributing them across a 512 MHz bandwidth. Signal demodulation of the 32 signals leverages a custom IF board for up- and down-conversion

²SRIM 2013 software package, <https://www.srim.org>

combined with a Software Defined Radio (SDR) implemented in the FPGA of a Reconfigurable Open Architecture Computing Hardware (ROACH2) board [41] equipped with ADC/DAC modules. Probe tones are amplified at 4 K by a LNA HEMT amplifier.

References

- J.J. Simpson, *Physical Review D* **23**(3), 649 (1981). DOI 10.1103/PhysRevD.23.649
- A. De Rújula, M. Lusignoli, *Physics Letters B* **118**(4-6), 429 (1982). DOI 10.1016/0370-2693(82)90218-0
- A. Hime, J.J. Simpson, *Physical Review D* **39**(7), 1837 (1989). DOI 10.1103/PhysRevD.39.1837
- E. Laegsgaard, J.U. Andersen, P.G. Hansen, A. De Rújula, B. Jonson, H.L. Ravn, in *7. International Conference on Atomic Masses and Fundamental Constants (AMCO-7) (1)*, ed. by O. Klepper (1984), THD-Schriftenreihe Wissenschaft Und Technik
- F.X. Hartmann, R.A. Naumann, *Nuclear Instruments and Methods in Physics Research Section A: Accelerators, Spectrometers, Detectors and Associated Equipment* **313**(1), 237 (1992). DOI 10.1016/0168-9002(92)90102-A
- A. Franklin, *Reviews of Modern Physics* **67**(2), 457 (1995). DOI 10.1103/RevModPhys.67.457
- A. Nucciotti, *Advances in High Energy Physics* **2016**, 1 (2016). DOI 10.1155/2016/9153024
- L. Erhardt, D. Deptuck, J. Harrison, *Nuclear Instruments and Methods in Physics Research Section A: Accelerators, Spectrometers, Detectors and Associated Equipment* **444**(1-2), 92 (2000). DOI 10.1016/S0168-9002(99)01336-4
- M.M. Lowry, D. Deptuck, I.C. Girit, *Journal of Low Temperature Physics* **93**(3-4), 239 (1993). DOI 10.1007/BF00693426
- F. Fontanelli, M. Galeazzi, F. Gatti, A.M. Swift, S. Vitale, *Nuclear Instruments and Methods in Physics Research Section A: Accelerators, Spectrometers, Detectors and Associated Equipment* **421**(3), 464 (1999). DOI 10.1016/S0168-9002(98)01201-7
- M. Sisti, C. Arnaboldi, C. Brofferio, G. Ceruti, O. Cremonesi, E. Fiorini, A. Giuliani, B. Margesin, L. Martensson, A. Nucciotti, M. Pavan, G. Pessina, S. Pirro, E. Previtali, L. Soma, M. Zen, *Nuclear Instruments and Methods in Physics Research Section A: Accelerators, Spectrometers, Detectors and Associated Equipment* **520**(1-3), 125 (2004). DOI 10.1016/j.nima.2003.11.273
- F. Gatti, P. Meunier, C. Salvo, S. Vitale, *Physics Letters B* **398**(3-4), 415 (1997). DOI 10.1016/S0370-2693(97)00239-6
- L. Gastaldo, P. Manfrinetti, F. Gatti, G. Gallinaro, D. Pergolesi, M.R. Gomes, M. Razeti, S. Dussoni, P. Repetto, R. Valle, *Nuclear Instruments and Methods in Physics Research Section A: Accelerators, Spectrometers, Detectors and Associated Equipment* **520**(1), 224 (2004). DOI 10.1016/j.nima.2003.11.250
- M.P. Croce, M.W. Rabin, V. Mocko, G.J. Kunde, E.R. Birnbaum, E.M. Bond, J.W. Engle, A.S. Hoover, F.M. Nortier, A.D. Pollington, W.A. Taylor, N.R. Weisse-Bernstein, L.E. Wolfsberg, J.P. Hays-Wehle, D.R. Schmidt, D.S. Swetz, J.N. Ullom, T.E. Barnhart, R.J. Nickles, *Journal of Low Temperature Physics* **184**(3-4), 958 (2016). DOI 10.1007/s10909-015-1451-2
- L. Gastaldo, K. Blaum, K. Chrysalidis, T. Day Goodacre, A. Domula, M. Door, H. Dorrer, Ch.E. Düllmann, K. Eberhardt, S. Eliseev, C. Enss, A. Faessler, P. Filianin, A. Fleischmann, D. Fonnesu, L. Gamer, R. Haas, C. Hassel, D. Hengstler, J. Jochum, K. Johnston, U. Kebschull, S. Kempf, T. Kieck, U. Köster, S. Lahiri, M. Maiti, F. Mantegazzini, B. Marsh, P. Neroutsos, Yu.N. Novikov, P.C.O. Ranitzsch, S. Rothe, A. Rischka, A. Saenz, O. Sander, F. Schneider, S. Scholl, R.X. Schüssler, Ch. Schweiger, F. Simkovic, T. Stora, Z. Szücs, A. Türlér, M. Veinhard, M. Weber, M. Wegner, K. Wendt, K. Zuber, *The European Physical Journal Special Topics* **226**(8), 1623 (2017). DOI 10.1140/epjst/e2017-70071-y
- B. Alpert, M. Balata, D. Bennett, M. Biasotti, C. Boragno, C. Brofferio, V. Ceriale, D. Corsini, P.K. Day, M. De Gerone, R. Dressler, M. Faverezani, E. Ferri, J. Fowler, F. Gatti, A. Giachero, J. Hays-Wehle, S. Heinitz, G. Hilton, U. Köster, M. Lusignoli, M. Maino, J. Mates, S. Nisi, R. Nizzolo, A. Nucciotti, G. Pessina, G. Pizzigoni, A. Puiu, S. Ragazzi, C. Reintsema, M.R. Gomes, D. Schmidt, D. Schumann, M. Sisti, D. Swetz, F. Terranova, J. Ullom, *The European Physical Journal C* **75**(3), 112 (2015). DOI 10.1140/epjc/s10052-015-3329-5
- S. Friedrich, G.B. Kim, C. Bray, R. Cantor, J. Dilling, S. Fretwell, J.A. Hall, A. Lennarz, V. Lordi, P. Machule, D. McKeen, X. Mougeot, F. Ponce, C. Ruiz, A. Samanta, W.K. Warburton, K.G. Leach, *Physical Review Letters* **126**(2), 021803 (2021). DOI 10.1103/PhysRevLett.126.021803
- S. Fretwell, K.G. Leach, C. Bray, G.B. Kim, J. Dilling, A. Lennarz, X. Mougeot, F. Ponce, C. Ruiz, J. Stackhouse, S. Friedrich, *Physical Review Letters* **125**(3), 032701 (2020). DOI 10.1103/PhysRevLett.125.032701
- K.E. Koehler, *Applied Sciences* **11**(9), 4044 (2021). DOI 10.3390/app11094044
- Y.C. Lee, H.B. Kim, H.L. Kim, S.K. Kim, Y.H. Kim, D.H. Kwon, H.S. Lim, H.S. Park, K.R. Woo, Y.S. Yoon, *Journal of Low Temperature Physics* **209**(5), 919

- (2022). DOI 10.1007/s10909-022-02879-6
21. K. Irwin, G. Hilton, in *Cryogenic Particle Detection*, ed. by C. Enss, Topics in Applied Physics (Springer, Berlin, Heidelberg, 2005), pp. 63–150. DOI 10.1007/10933596_3
 22. B. Alpert, D. Becker, D. Bennet, M. Biasotti, M. Borghesi, G. Gallucci, M. De Gerone, M. Faverzani, E. Ferri, J. Fowler, J. Gard, A. Giachero, J. Hays-Wehle, G. Hilton, J. Mates, A. Nucciotti, A. Orlando, G. Pessina, A. Puiu, C. Reintsema, D. Schmidt, D. Swetz, J. Ullom, L. Vale, *The European Physical Journal C* **79**(4), 304 (2019). DOI 10.1140/epjc/s10052-019-6814-4
 23. M. Faverzani, B. Alpert, D. Backer, D. Bennet, M. Biasotti, C. Brofferio, V. Ceriale, G. Ceruti, D. Corsini, P.K. Day, et al., *Journal of Low Temperature Physics* **184**, 922–929 (2016)
 24. J.P. Hays-Wehle, D.R. Schmidt, J.N. Ullom, D.S. Swetz, *Journal of Low Temperature Physics* **184**(1-2), 492 (2016). DOI 10.1007/s10909-015-1416-5
 25. J.N. Ullom, W.B. Doriese, G.C. Hilton, J.A. Beall, S. Deiker, W.D. Duncan, L. Ferreira, K.D. Irwin, C.D. Reintsema, L.R. Vale, *Applied Physics Letters* **84**(21), 4206 (2004). DOI 10.1063/1.1753058
 26. D. McCammon, in *Cryogenic Particle Detection*, ed. by C. Enss, Topics in Applied Physics (Springer, Berlin, Heidelberg, 2005), pp. 1–34. DOI 10.1007/10933596_1
 27. A. Nucciotti, *The European Physical Journal C* **74**(11), 3161 (2014). DOI 10.1140/epjc/s10052-014-3161-3
 28. M. Borghesi, M. Faverzani, C. Ferrari, E. Ferri, A. Giachero, A. Nucciotti, L. Origo, *The European Physical Journal C* **82**(5), 421 (2022). DOI 10.1140/epjc/s10052-022-10379-w
 29. M. Krusius, A.C. Anderson, B. Holmström, *Physical Review* **177**(2), 910 (1969). DOI 10.1103/PhysRev.177.910
 30. G. Williams, L.L. Hirst, *Physical Review* **185**(2), 407 (1969). DOI 10.1103/PhysRev.185.407
 31. L. Gastaldo, P.O. Ranitzsch, F. von Seggern, J.P. Porst, S. Schäfer, C. Pies, S. Kempf, T. Wolf, A. Fleischmann, C. Enss, A. Herlert, K. Johnston, *Nuclear Instruments and Methods in Physics Research Section A: Accelerators, Spectrometers, Detectors and Associated Equipment* **711**, 150 (2013). DOI 10.1016/j.nima.2013.01.027
 32. M. Herbst, A. Reifenberger, C. Velte, H. Dorrer, C.E. Düllmann, C. Enss, A. Fleischmann, L. Gastaldo, S. Kempf, T. Kieck, U. Köster, F. Mantegazzini, K. Wendt, *Journal of Low Temperature Physics* **202**(1-2), 106 (2021). DOI 10.1007/s10909-020-02531-1
 33. B.K. Alpert, M. Balata, D.T. Becker, D.A. Bennett, M. Borghesi, P. Campana, R. Carobene, M.D. Gerone, W.B. Doriese, M. Faverzani, L.F. Barusso, E. Ferri, J.W. Fowler, G. Gallucci, S. Gamba, J.D. Gard, F. Gatti, A. Giachero, M. Gobbo, U. Köster, D. Labranca, M. Lusignoli, P. Manfrinetti, J.A.B. Mates, E. Maugeri, R. Moretti, S. Nisi, A. Nucciotti, G.C. O’Neil, L. Origo, G. Pessina, S. Ragazzi, C.D. Reintsema, D.R. Schmidt, D. Schumann, D.S. Swetz, Z. Talip, J.N. Ullom, L.R. Vale. Most stringent bound on electron neutrino mass obtained with a scalable low temperature microcalorimeter array (2025). DOI 10.48550/arXiv.2503.19920
 34. E. Gatti, P.F. Manfredi, *La Rivista del Nuovo Cimento* **9**(1), 1 (1986). DOI 10.1007/BF02822156
 35. M. Borghesi, *Toward the first neutrino mass measurement of Holmes*. Ph.D. thesis, University of Milano-Bicocca, Milano, Italy (2022)
 36. G. Hölzer, M. Fritsch, M. Deutsch, J. Härtwig, E. Förster, *Physical Review A* **56**(6), 4554 (1997). DOI 10.1103/PhysRevA.56.4554
 37. E. Ferri, S. Kraft-Bermuth, A. Monfardini, A. Nucciotti, D. Schaeffer, M. Sisti, *Eur. Phys. J. A* **48**, 131 (2012). DOI 10.1140/epja/i2012-12131-5
 38. S. Heinitz, N. Kivel, D. Schumann, U. Köster, M. Balata, M. Biasotti, V. Ceriale, M. De Gerone, M. Faverzani, E. Ferri, G. Gallucci, F. Gatti, A. Giachero, S. Nisi, A. Nucciotti, A. Orlando, G. Pessina, A. Puiu, S. Ragazzi, *PLOS ONE* **13**(8), e0200910 (2018). DOI 10.1371/journal.pone.0200910
 39. M. De Gerone, A. Bevilacqua, M. Borghesi, N. Cerboni, G. Ceruti, G. De Bodin De Galembert, M. Faverzani, M. Fedkevych, E. Ferri, G. Gallucci, F. Gatti, A. Giachero, E. Maugeri, P. Manfrinetti, A. Nucciotti, L. Parodi, G. Pessina, S. Ragazzi, D. Schumann, F. Siccardi, *Nuclear Instruments and Methods in Physics Research, Section A: Accelerators, Spectrometers, Detectors and Associated Equipment* **1051** (2023). DOI 10.1016/j.nima.2023.168168
 40. D. Becker, D. Bennett, M. Biasotti, M. Borghesi, V. Ceriale, M.D. Gerone, M. Faverzani, E. Ferri, J. Fowler, G. Gallucci, J. Gard, A. Giachero, J. Hays-Wehle, G. Hilton, J. Mates, A. Nucciotti, A. Orlando, G. Pessina, A. Puiu, C. Reintsema, D. Schmidt, D. Swetz, J. Ullom, L. Vale, *Journal of Instrumentation* **14**(10), P10035 (2019). DOI 10.1088/1748-0221/14/10/P10035
 41. S. McHugh, B.A. Mazin, B. Serfass, S. Meeker, K. O’Brien, R. Duan, R. Raffanti, D. Werthimer, *Review of Scientific Instruments* **83**(4), 044702 (2012). DOI 10.1063/1.3700812